Supporting Information for:

Catalytic NO Activation and NO–H_2 Reaction Pathways

David D. Hibbitts[1], Romel Jiménez[1,4], Masayuki Yoshimura[1,3], Brian Weiss[1,5], Enrique Iglesia[1,2]*

[1]Department of Chemical Engineering, University of California, Berkeley (USA)

[2]E.O. Lawrence Berkeley National Laboratory, Berkeley, CA (USA)

Current Address: [3]Corporate R&D Center (Toke), Showa Denko K.K. (Japan);

[4]Department of Chemical Engineering, University of Concepcion, Concepcion (Chile);

[5]Corporate Research Strategic Lab, Exxon Mobil Research and Eng. Co. Annandale, NJ (USA)

* Corresponding author: iglesia@berkeley.edu

Table of Contents

List of Figures and Tables

S1. Details of DFT calculations of thermochemical properties

The enthalpy of a given state can be written as the sum of the DFT-derived energy (E_0), zero-point vibrational enthalpy (*ZPVE*) and vibrational, translational and rotational enthalpy (H_{vib}, H_{trans} and H_{rot}):

$$H = E_0 + ZPVE + H_{vib} + H_{trans} + H_{rot} \quad \text{(S1)}$$

similarly, the free energy of a state can be written as:

$$G = E_0 + ZPVE + G_{vib} + G_{trans} + G_{rot} \quad \text{(S2)}$$

and entropy can be determined for a state with a known *H* and *G* at a given *T*:

$$S = \frac{H - G}{T} \quad \text{(S3)}$$

For calculations which include a periodic Pt(111) surface (including adsorbed species and transition states on that surface), there are no translational or rotational degrees of freedom and DFT-derived vibrational frequencies can be used to determine the *ZPVE*, H_{vib} and G_{vib} shown in Eqns. S4-6.

$$ZPVE = \sum_i (½ \nu_i h) \quad \text{(S4)}$$

$$H_{vib} = \sum_i \left(\frac{\nu_i h e^{\frac{-\nu_i h}{kT}}}{1 - e^{\frac{-\nu_i h}{kT}}} \right) \quad \text{(S5)}$$

$$G_{vib} = \sum_i \left(-kT \ln \frac{1}{1 - e^{\frac{-\nu_i h}{kT}}} \right) \quad \text{(S6)}$$

where ν_i is the frequency, *h* is Planck's constant, *k* is Boltzmann's constant.

Gas-phase molecules have translational and rotational degrees of freedom; thus H_{trans}, H_{rot}, G_{trans} and G_{rot} must also be computed: [1]

[1] Statistical Mechanics", D. A. McQuarrie, 2000, University Science Books, Sausolito, CA.

$$H_{trans} = {}^{5}/_{2}\, kT \tag{S7}$$

$$H_{rot,linear} = kT \tag{S8}$$

$$G_{trans} = -kT \ln\left[\left(\frac{2\pi MkT}{h^2}\right)^{3/2} V\right] \tag{S9}$$

$$G_{rot} = -kT \ln\left[\frac{\pi^{1/2}}{\sigma}\left(\frac{T^3}{\theta_x\theta_y\theta_z}\right)^{1/2}\right] \tag{S10}$$

$$\theta_i = \frac{h^2}{8\pi^2 I_i k} \tag{S11}$$

where I_i is the moment of inertia about axes x, y or z and σ is the symmetry number of the molecule, 2 for H_2, 1 for NO.

S2. Effects of products on NO reactions with H_2 on Pt/Al_2O_3

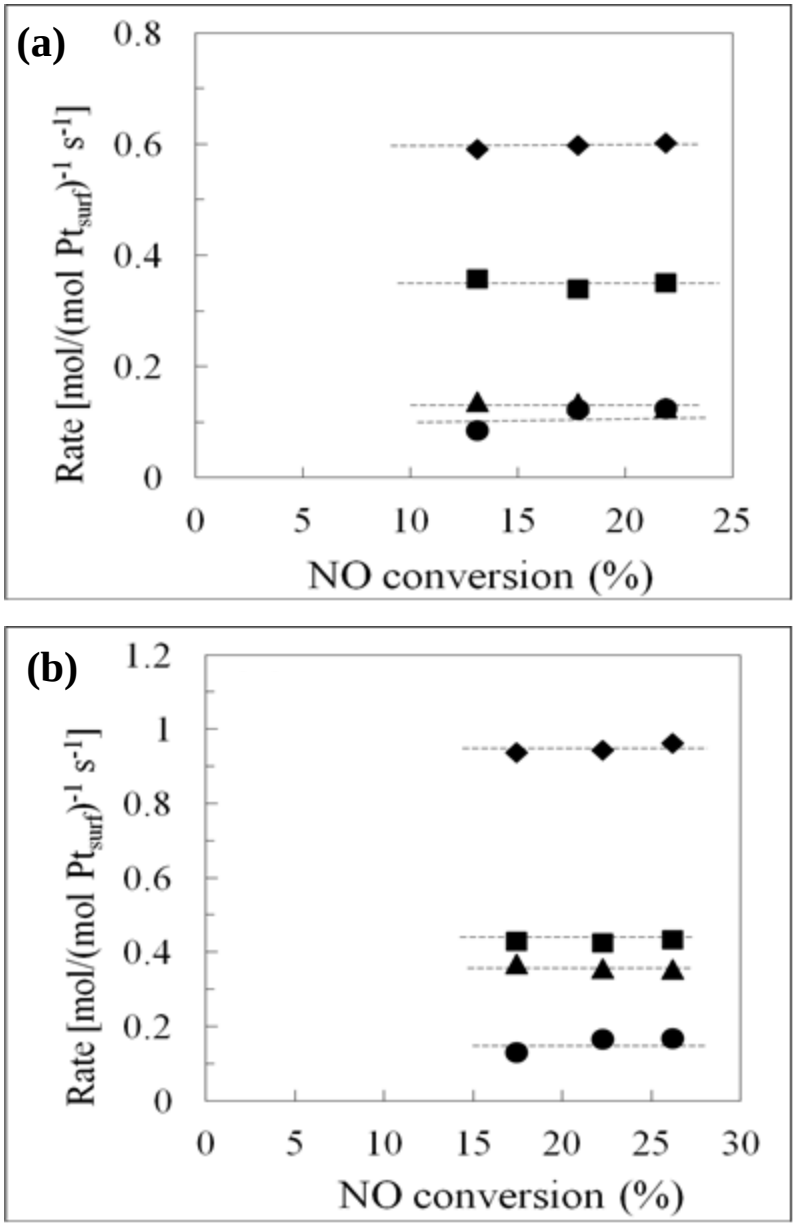

Figure S1. Effect of varying the space velocity on NO conversion rate at (a) 423 K and (b) 453 K during NO/H_2 reactions on $0.6\%Pt/Al_2O_3$ (0.25 dispersion), (◆) NO consumption, (■) N_2O formation (x 2), (●) N_2 formation (x 2), (▲) NH_3 formation (0.3 kPa NO; 1.5 kPa H_2).

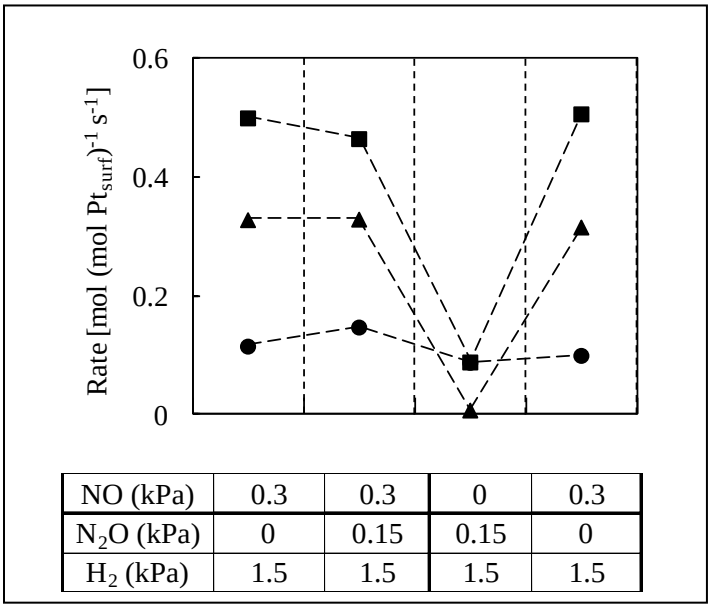

NO (kPa)	0.3	0.3	0	0.3
N_2O (kPa)	0	0.15	0.15	0
H_2 (kPa)	1.5	1.5	1.5	1.5

Figure S2. Effect of product N_2O addition on NO conversion rate at 453 K during NO/H_2 reactions on 0.6%Pt/Al_2O_3 (0.25 dispersion), (■) N_2O formation (x2), (●) N_2 formation (x2), (▲) NH_3 formation. (100 ml/min, 0.3 kPa NO, 0.4 kPa NH_3, 0.6 kPa H_2).

S3. Rate equation and kinetic parameter fitting.

In this section, for brevity, (NO) indicates NO pressure (P_{NO} elsewhere) and (H_2) indicates H_2 pressure (P_{H2} elsewhere).

A variety of rate equations were fitted to the kinetic data shown in Figs. 4-5 to determine which rate equation is most consistent with the measured data. For this section, first we begin with a rate equation (Eq. S12) first-order in NO and H_2 with (*), NO* and H* as MASI (Eq. 12 in the main text). To avoid disproportionately weighting data obtained at higher rates, relative errors (RE, Eq. S13) were minimized rather than absolute error minimization typically performed by least-squares regression techniques.

$$r = \frac{\alpha\prime(NO)(H_2)}{\left[1+K_{NO}(NO)+K_{H_2}^{0.5}(H_2)^{0.5}\right]^2} \tag{S12}$$

$$RE = \left|\frac{r_i - r}{r}\right| 100 \tag{S13}$$

We can generalize this rate equation by adding parameters (which we will constrain to be integer values) for the reaction orders in NO ($N°$) and H ($H°$) in the numerator, as well as the number of catalyst sites required to form the kinetically-relevant transition state (ℓ).

$$r = \frac{\alpha\prime(NO)^{N°}(H_2)^{\frac{H°}{2}}}{\left[1+K_{NO}(NO)+K_{H_2}^{0.5}(H_2)^{0.5}\right]^{\ell}} \tag{S14}$$

Table S1 summarizes the kinetic parameters (α', K_{NO}, K_{H2}) and shows the sum of relative errors (SRE) obtained from the fits for $N°$ from 1 to 2, $H°$ from 1 to 3 and ℓ from 1 to 3.

Table S1. Comparison of parameter fitting on different forms of Equation S3.

			383 K				423 K				453 K				
			α'	K_{NO}	K_{H2}	*SRE*	α'	K_{NO}	K_{H2}	*SRE*	α'	K_{NO}	K_{H2}	*SRE*	*Total*
N°	*H°*	ℓ	$s^{-1}\,kPa^{-2}$	kPa^{-1}	kPa^{-1}		$s^{-1}\,kPa^{-2}$	kPa^{-1}	kPa^{-1}		$s^{-1}\,kPa^{-2}$	kPa^{-1}	kPa^{-1}		*SRE*
1	1	1	3.24×10^{2}	1.23×10^{3}	4.59×10^{2}	223	3.03×10^{2}	5.45×10^{2}	2.53×10^{2}	122	2.92×10^{2}	3.26×10^{2}	1.74×10^{2}	232	577
1	1	2	5.81×10^{0}	5.26×10^{0}	8.62×10^{-3}	214	6.87×10^{0}	2.73×10^{0}	1.33×10^{-2}	169	7.69×10^{0}	1.80×10^{0}	1.76×10^{-2}	110	502
1	1	3	4.42×10^{0}	2.34×10^{0}	1.50×10^{-3}	222	5.26×10^{0}	1.20×10^{0}	2.73×10^{-3}	229	5.91×10^{0}	7.82×10^{-1}	3.99×10^{-3}	89	540
1	2	1	2.61×10^{3}	1.23×10^{4}	5.28×10^{5}	828	1.03×10^{3}	7.64×10^{2}	1.48×10^{5}	526	5.76×10^{2}	1.31×10^{2}	6.60×10^{4}	420	1775
1	**2**	**2**	$\mathbf{6.83\times10^{2}}$	$\mathbf{7.65\times10^{1}}$	$\mathbf{6.96\times10^{1}}$	**151**	$\mathbf{4.65\times10^{2}}$	$\mathbf{3.05\times10^{1}}$	$\mathbf{4.42\times10^{1}}$	**92**	$\mathbf{3.66\times10^{2}}$	$\mathbf{1.70\times10^{1}}$	$\mathbf{3.32\times10^{1}}$	**136**	**380**
1	2	3	1.66×10^{1}	4.65×10^{0}	2.51×10^{-1}	162	1.97×10^{1}	2.54×10^{0}	2.82×10^{-1}	100	2.22×10^{1}	1.73×10^{0}	3.03×10^{-1}	182	443
1	3	1	1.28×10^{4}	5.17×10^{4}	2.53×10^{7}	1467	6.34×10^{3}	9.76×10^{3}	4.90×10^{6}	497	4.09×10^{3}	3.39×10^{3}	1.73×10^{6}	1216	3180
1	3	2	3.74×10^{10}	4.51×10^{5}	1.40×10^{10}	740	4.01×10^{9}	4.03×10^{4}	1.54×10^{9}	514	9.79×10^{8}	8.72×10^{3}	3.80×10^{8}	481	1736
1	3	3	1.67×10^{3}	2.41×10^{1}	3.18×10^{1}	227	1.08×10^{3}	1.06×10^{1}	2.18×10^{1}	104	8.26×10^{2}	6.30×10^{0}	1.71×10^{1}	169	500
2	1	1	6.91×10^{5}	4.11×10^{5}	1.07×10^{6}	980	1.55×10^{5}	7.47×10^{4}	2.79×10^{5}	762	6.06×10^{4}	2.53×10^{4}	1.19×10^{5}	377	2119
2	1	2	1.43×10^{7}	7.52×10^{3}	2.21×10^{3}	213	2.74×10^{6}	2.18×10^{3}	1.07×10^{3}	135	9.70×10^{5}	9.98×10^{2}	6.72×10^{2}	140	488
2	1	3	2.37×10^{2}	1.10×10^{1}	9.09×10^{-3}	203	1.81×10^{2}	6.58×10^{0}	1.31×10^{-2}	204	1.53×10^{2}	4.75×10^{0}	1.65×10^{-2}	115	522
2	2	1	7.28×10^{5}	7.09×10^{5}	2.10×10^{6}	1474	3.76×10^{4}	1.82×10^{4}	5.31×10^{5}	873	5.78×10^{3}	1.79×10^{3}	2.22×10^{5}	780	3127
2	2	2	6.98×10^{8}	5.10×10^{4}	4.02×10^{6}	671	9.51×10^{7}	1.15×10^{4}	9.55×10^{5}	533	2.70×10^{7}	4.46×10^{3}	3.84×10^{5}	405	1609
2	2	3	1.65×10^{4}	5.44×10^{1}	6.38×10^{0}	230	7.97×10^{3}	2.76×10^{1}	5.08×10^{0}	96	5.05×10^{3}	1.79×10^{1}	4.40×10^{0}	260	585
2	3	1	9.42×10^{6}	8.36×10^{6}	3.32×10^{5}	1860	2.35×10^{6}	1.70×10^{6}	9.51×10^{4}	803	9.82×10^{5}	6.22×10^{5}	4.30×10^{4}	1419	4081
2	3	2	1.43×10^{9}	6.48×10^{4}	2.95×10^{7}	1289	3.14×10^{8}	2.09×10^{4}	5.52×10^{6}	671	1.21×10^{8}	1.02×10^{4}	1.91×10^{6}	1149	3109
2	3	3	3.48×10^{9}	2.87×10^{3}	1.00×10^{5}	561	5.30×10^{8}	1.01×10^{3}	3.38×10^{4}	416	1.62×10^{8}	5.24×10^{2}	1.69×10^{4}	501	1478

Large adsorption constants for NO and H_2 (K_{NO}, K_{H2}) obtained for Eq. S12 indicate a vacancy coverage (θ_*) less than 0.09 at NO and H_2 pressures the kinetic data were measured at, with 68% of the rate data having a θ_* less than 0.05. Low vacancy coverages suggest that α', K_{NO}, and K_{H2} may be correlated, so a sensitivity analysis was performed to determine confidence intervals on the kinetic parameters. Figure S3 shows that as K_{H2} decreases from its optimized value of 6.96×10^{1} (with α' and K_{NO} optimized at each point), the SRE increases sharply, indicating a worsening fit, however, as K_{H2} increases, the resulting increase to the SRE is much more gradual, with the fit worsening by only ~10% over an increase in K_{H2} of multiple orders of magnitude. K_{NO} changes in a similar manner, indicating that a ratio of these two factors (β, Eq. S16 below) is unchanging over these conditions (Fig. S4) and similarly, the ratio of α' to K_{NO}^2 only slightly changes as K_{H2} is varied. It is impossible to define upper bounds on the values of K_{H2} and K_{NO} because K_{H2}, K_{NO} and α' are correlated as K_{H2} increases, however, we can confidently assign lower bounds, as indicated by the sharp increase in SRE when K_{H2} or K_{NO} is decreased beneath a value of 4 kPa^{-1} or 18 kPa^{-1}, respectively; because at lower values of K_{H2} or K_{NO}, the predicted coverage of vacancies is too high to be consistent with the kinetic data.

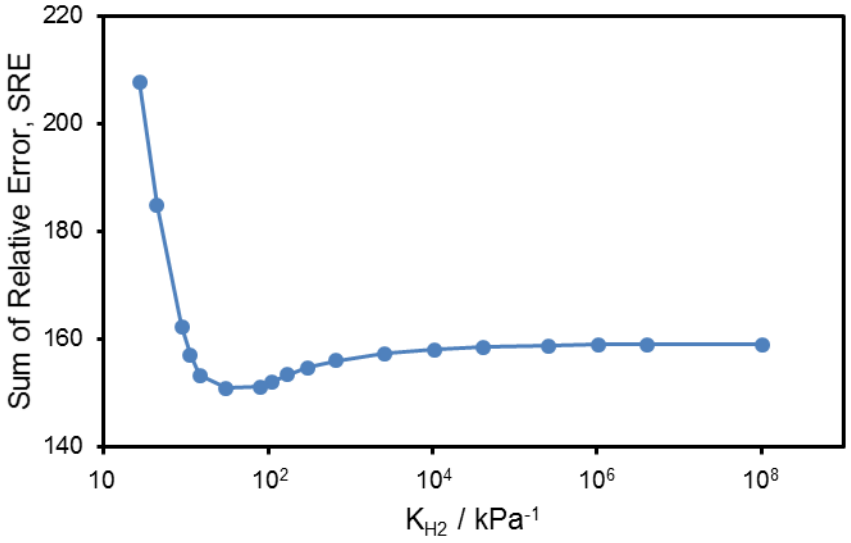

Figure S3. Change in the fit error (SRE) with K_{H2} (for each point, α and K_{NO} are optimized to minimize SRE).

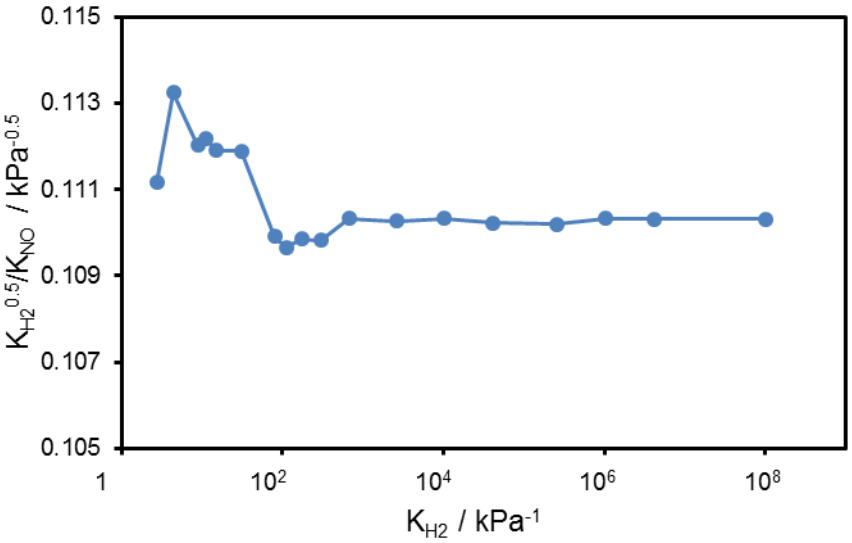

Figure S4. Change in the ratio of $K_{H2}^{0.5}$:K_{NO} (β) with K_{H2} (for each point, α and K_{NO} are optimized to minimize SRE).

At large values of K_{H2} and K_{NO}, the rate equation (Eq. S12) can be simplified by removing the 1 term (representing vacancies) from the denominator and introducing a new parameter (β, Eq. S16) representing the ratio of the root of K_{H2} to K_{NO}. Sensitivity analysis on these parameters (α, β) show a more typical response of rapidly increasing RSE values as either parameter is increased/decreased. Defining a confidence interval based on a 10% increase in RSE gives an α of 1.013 ± 0.032 and a β of 0.110 ± 0.006.

$$r = \frac{\alpha\prime(NO)(H_2)}{\left[K_{NO}(NO)+K_{H_2}^{0.5}(H_2)^{0.5}\right]^2} = \frac{\alpha(NO)(H_2)}{[(NO)+\beta(H_2)^{0.5}]^2} \quad \text{(S15)}$$

$$\beta = \frac{K_{H_2}^{0.5}}{K_{NO}} \quad \text{(S16)}$$

$$\alpha = \frac{\alpha\prime}{K_{NO}^2} \quad \text{(S17)}$$

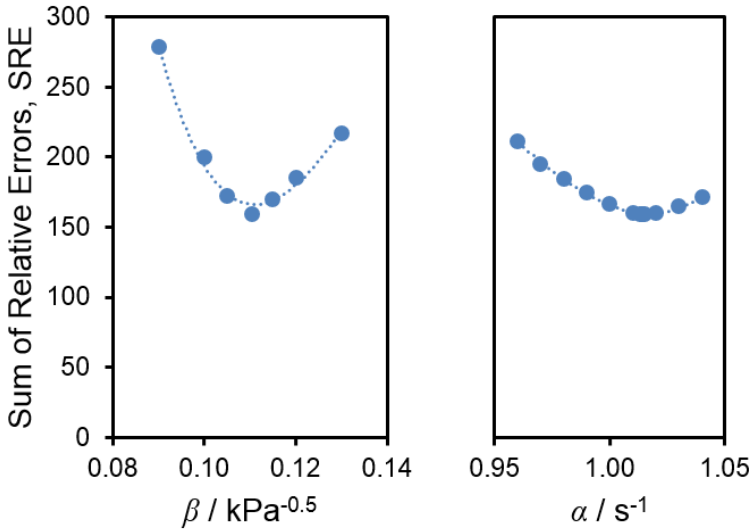

Figure S5. Change in the fit error (SRE) with β (left, for each point α was optimized) and with α (right, for each point β was optimized).

S4. H_2 and NO Adsorption Studies

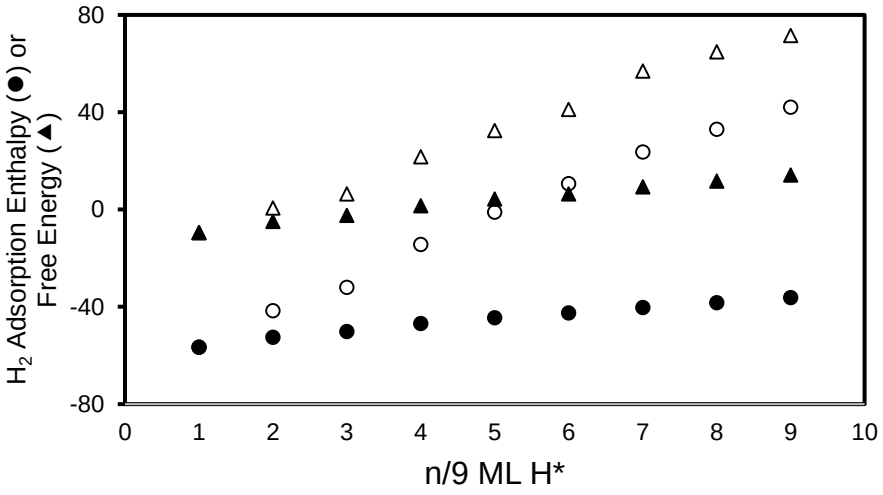

Figure S6. H_2 adsorption enthalpy (● or ○, *H)*, and free energy (▲ or △, *G*) on Pt(111) as a function of H* coverage. Closed symbols represent average adsorption energies of each H*, open symbols represent differential adsorption energies.

$\Delta H_{ads,H}$ and $\Delta G_{ads,H}$ increase with increasing H* coverage (Fig. S6), with $\Delta G_{ads,H}$ being larger (less favorable) than $\Delta H_{ads,H}$ due to the loss in entropy upon H* adsorption ($\Delta S_{ads,H} \leq$ -35 J mol^{-1} K^{-1}). Figure S6 displays energies for the most favorable configuration of H* on the surface, however, energies of many additional configurations were calculated (Figs. S7-S9). One H* on the surface (Fig. S7) prefers to bind to a 3-fold fcc site, with a slightly lower $\Delta H_{ads,H}$ than adsorption to an atop site (by 4 kJ mol^{-1}) and the same $\Delta G_{ads,H}$ (-5 kJ mol^{-1}), indicating H* has more entropy in an atop site. H* bound to 3-fold hcp sites was also considered, but was found to be less favorable than the 3-fold fcc site. H* prefers to bind at fcc sites at all coverages, unlike NO*, and H*-H* repulsions seem nearly independent of H* configuration (also unlike NO*) as shown by similar $\Delta H_{ads,H}$ and $\Delta G_{ads,H}$ values for various configurations of atop and fcc H* at each coverage (Figs. S7-S9). This indicates that H*-H* repulsion is primarily a through-metal process, in which the affinity of the metal towards adsorbates is slightly decreased with increasing coverage, unlike NO*-NO* repulsions, which have large through-metal and through-space contributions.

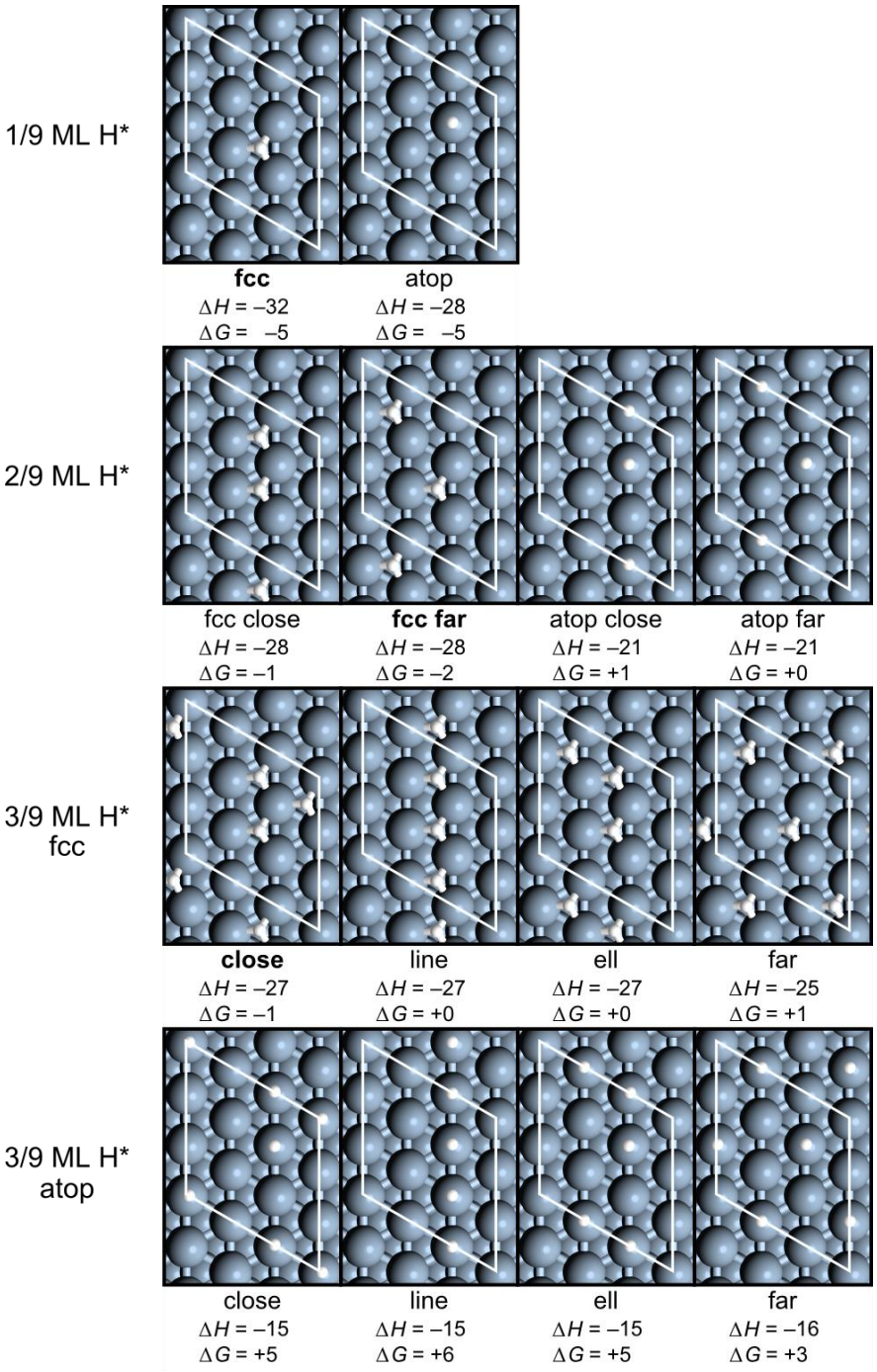

Figure S7. DFT-calculated structures and differential adsorption energies (based on the most stable configuration at lower coverage and ½ H_2(g) as the reference) of various H* configurations at 0 – 1/3 ML H*.

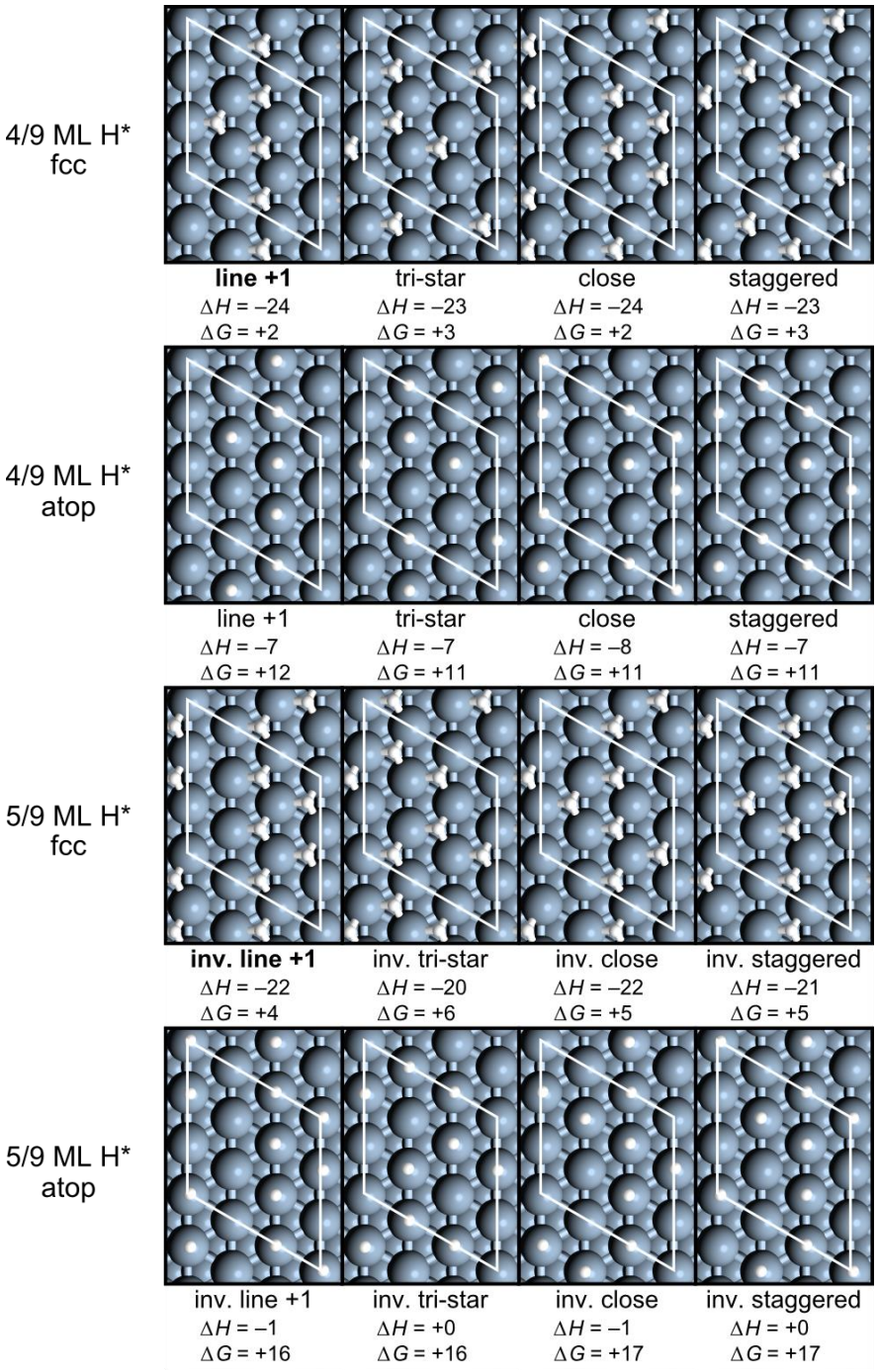

Figure S8. DFT-calculated structures and differential adsorption energies (based on the most stable configuration at lower coverage and ½ H_2(g) as the reference) of various H* configurations at 4/9 – 5/9 ML H*.

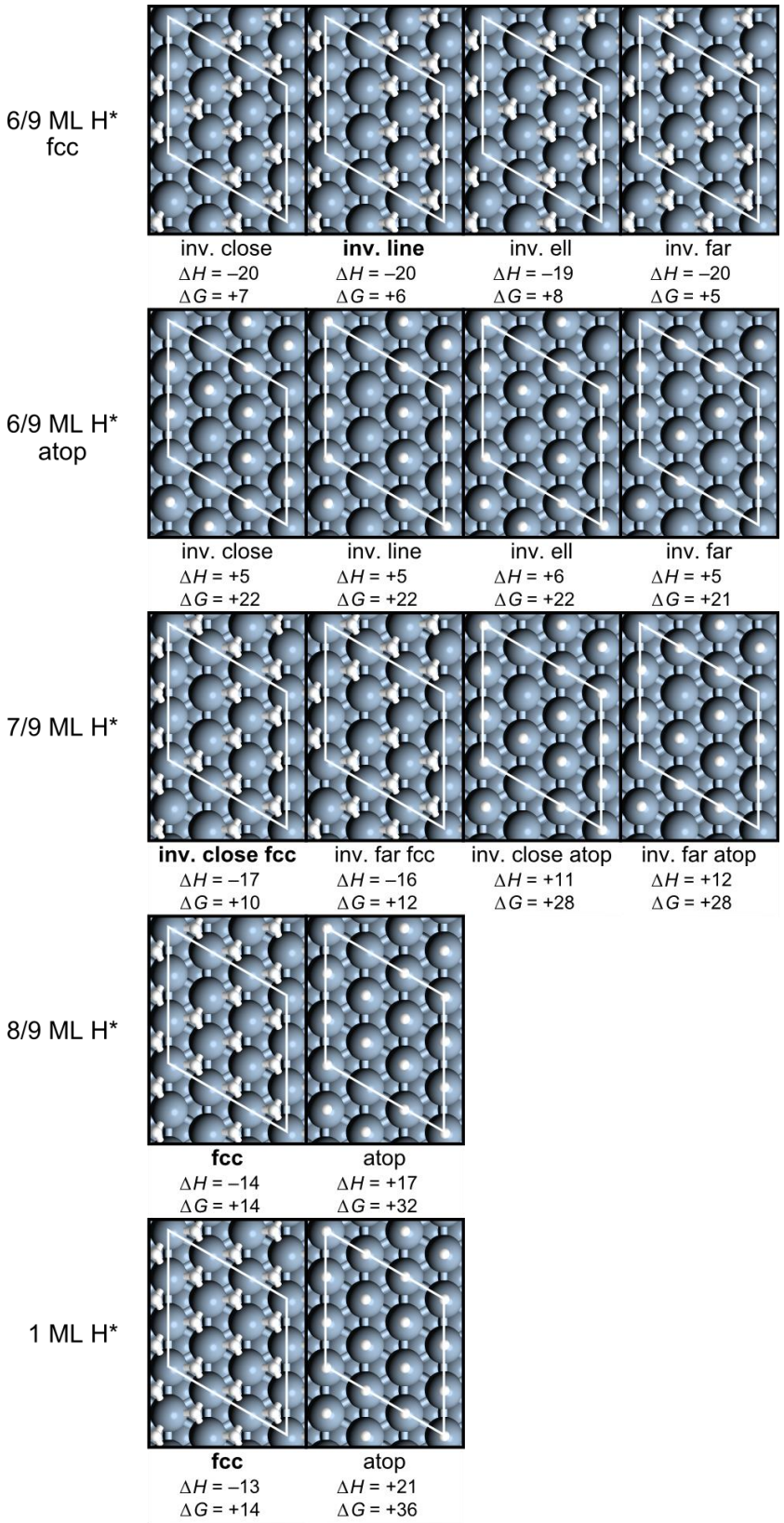

Figure S9. DFT-calculated structures and differential adsorption energies (based on the most stable configuration at lower coverage and ½ H_2(g) as the reference) of various H* configurations at 6/9 – 1 ML H*.

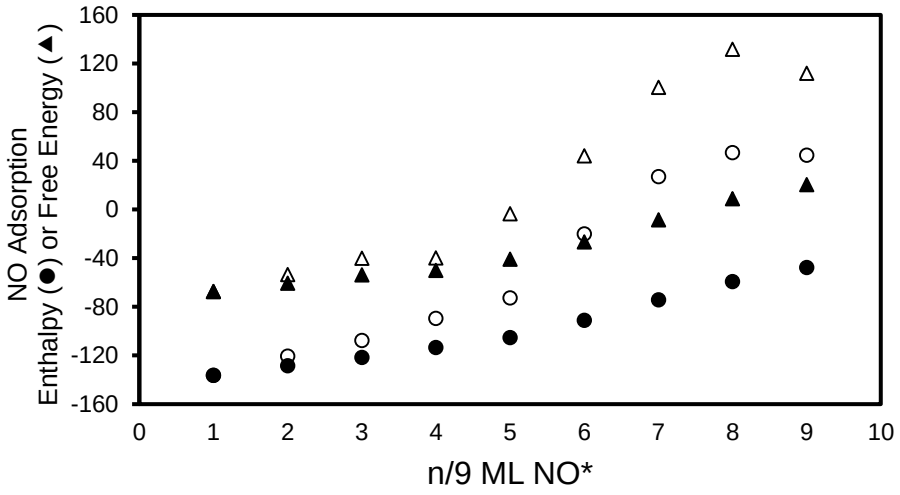

Figure S10. NO adsorption enthalpy (● or ○, *H)*, and free energy (▲ or △, *G*) on Pt(111) as a function of NO* coverage. Closed symbols represent average adsorption energies of each NO*, open symbols represent differential adsorption energies.

$\Delta H_{ads,NO}$ and $\Delta G_{ads,NO}$ increase with increasing NO* coverage (Fig. S10), with $\Delta G_{ads,NO}$ being larger (less favorable) than $\Delta H_{ads,NO}$ due to the loss in entropy upon NO* adsorption ($\Delta S_{ads,NO} \leq$ -139 J mol^{-1} K^{-1}). Figure S10 displays energies for the most favorable configuration of NO* on the surface, however, energies of many additional configurations were calculated (Figs. S7-S9). One NO* on the surface (Fig. S11) prefers to bind to a 3-fold fcc site, with a slightly lower $\Delta G_{ads,NO}$ than adsorption to an atop site and significantly lower $\Delta H_{ads,NO}$. NO* bound to 3-fold hcp sites was also considered, but was found to be less favorable than the 3-fold fcc site. NO* prefer to bind to 3-fold fcc sites at 2/9 and 3/9 ML as well, arranging themselves in configurations which avoid metal-atom-sharing between adsorbates. At 4/9 ML NO*, if all NO* are bound to 3-fold sites, metal-atom sharing is unavoidable, instead, two NO* occupy atop sites, resulting in eight total M-N bonds, with a non-interacting metal site, which is filled with an atop NO* at 5/9 ML (Fig. S12). At 6/9 ML NO*, only one NO* can bind 3-fold while preventing metal-atom-sharing, with the five remaining NO* occupying atop sites, resulting in eight total M-N bonds, with one non-interacting metal site, which is filled with an atop NO* at 7/9 ML (Fig. S13). At 8/9 ML, zero NO* can bind 3-fold while avoiding metal-atom-sharing, so all eight NO* bind atop, resulting in eight total M-N bonds. At 1 ML, the surface is filled with atop-bound NO* species, which are more stable when disordered, rather than aligned (Fig. S13).

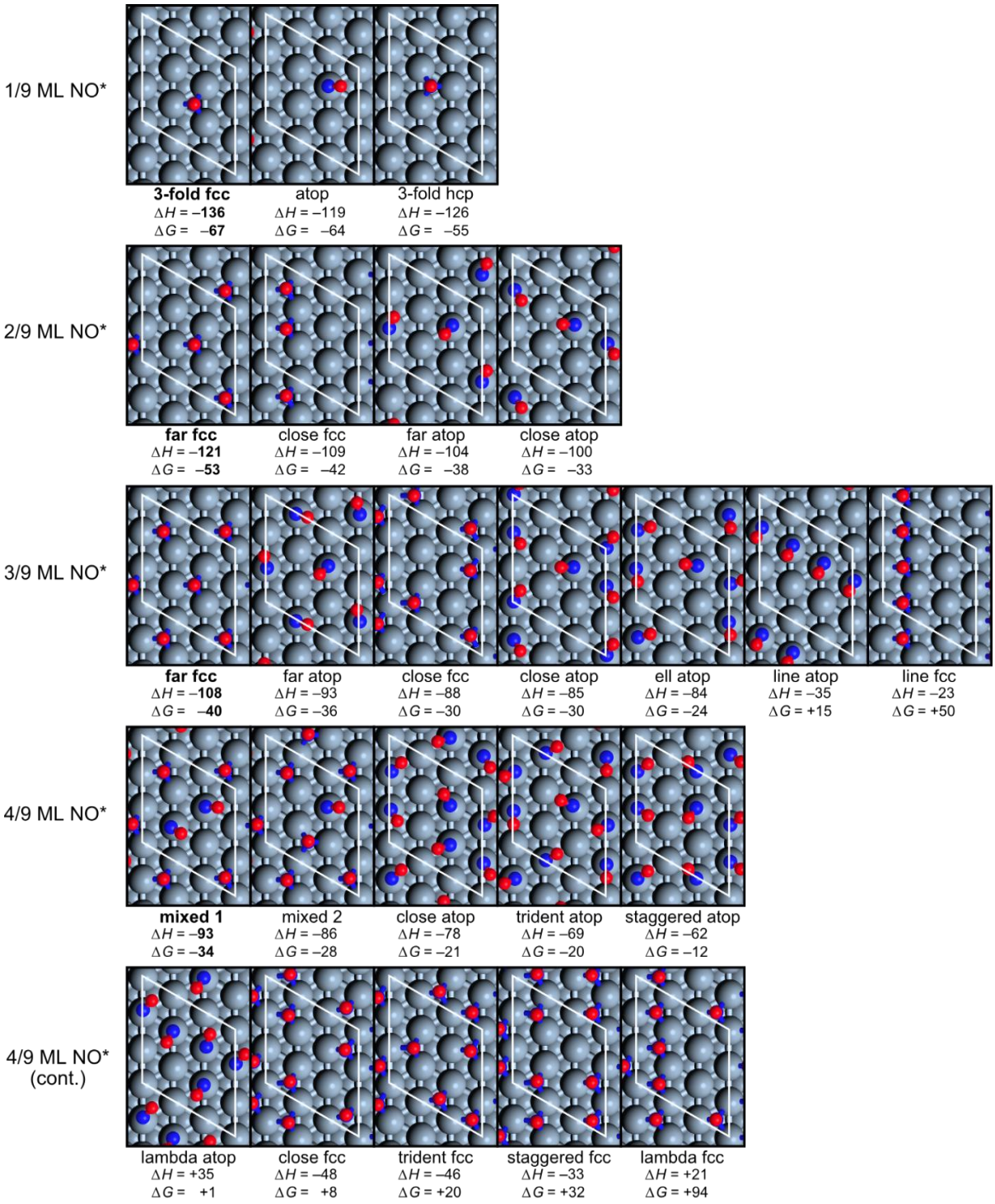

Figure S11. DFT-calculated structures and differential adsorption energies (based on the most stable configuration at lower coverage) of various NO* configurations at 1/9 – 4/9 ML NO*.

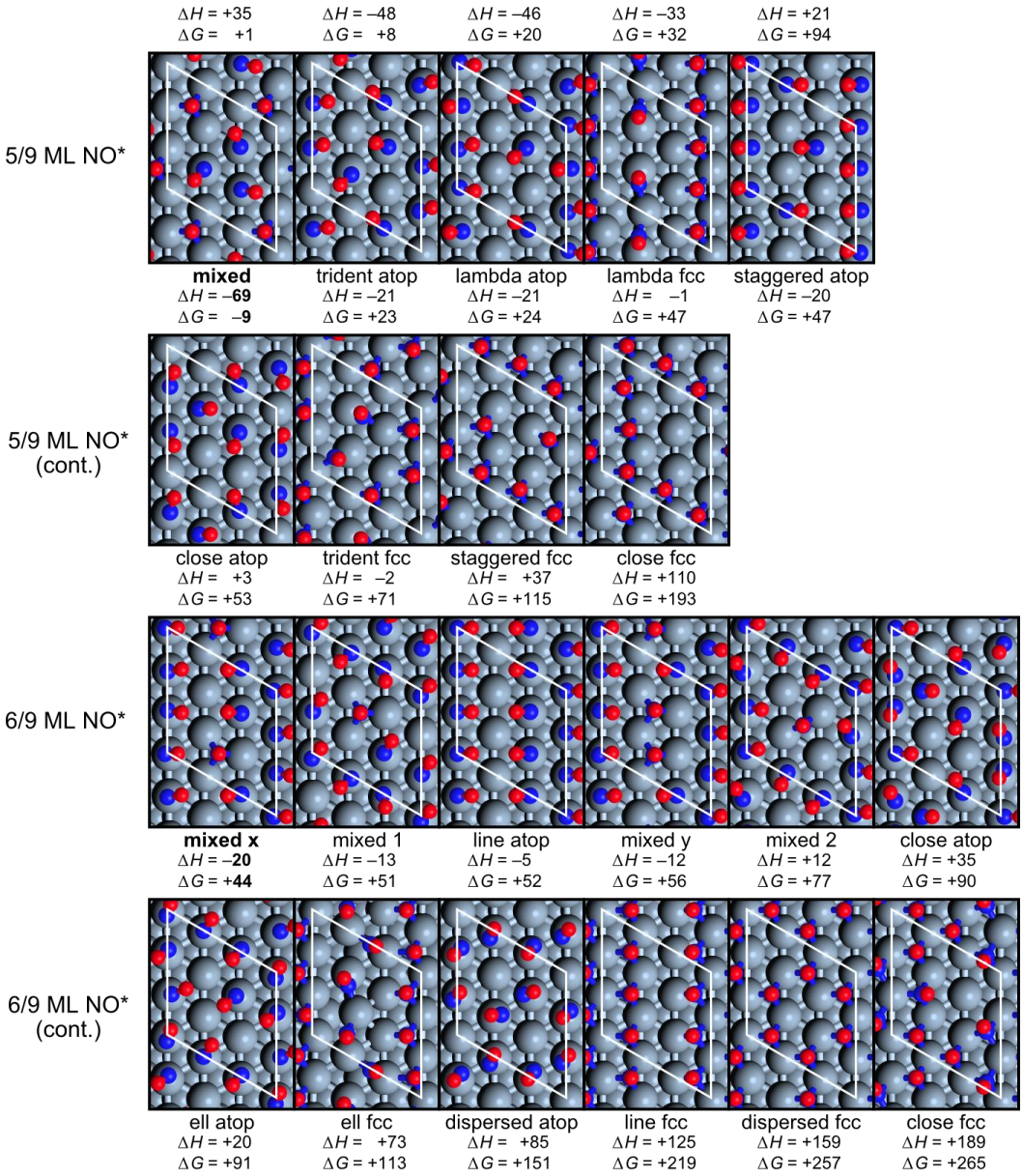

Figure S12. DFT-calculated structures and differential adsorption energies (based on the most stable configuration at lower coverage) of various NO* configurations at 5/9 – 6/9 ML NO*.

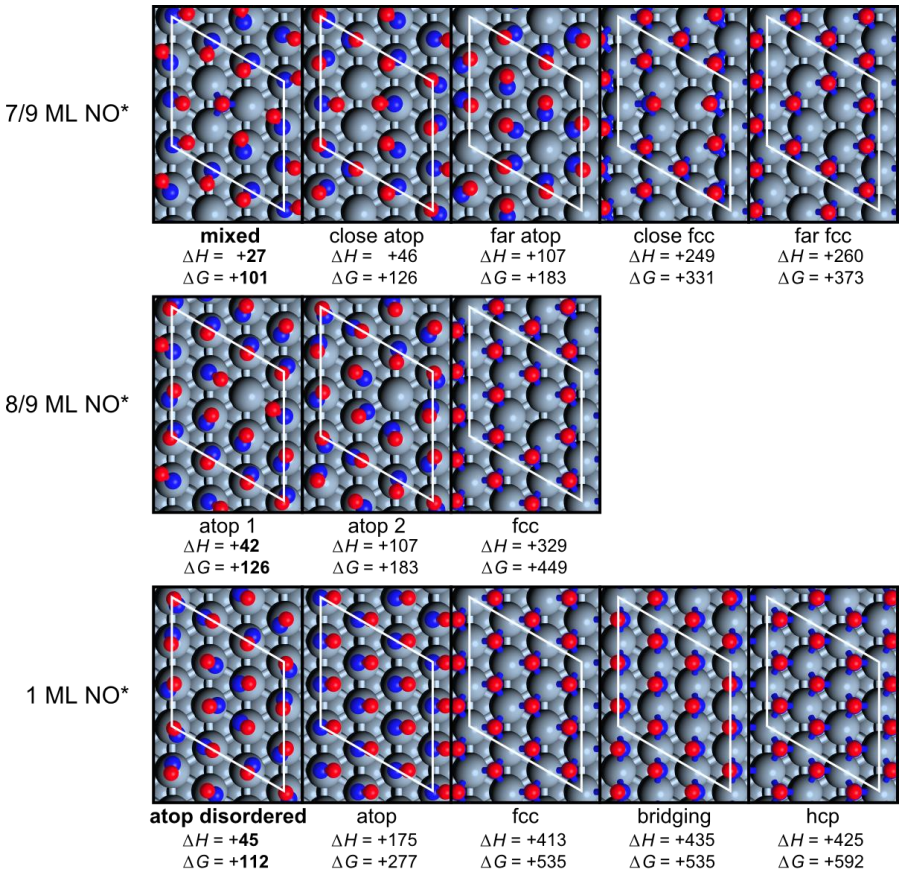

Figure S13. DFT-calculated structures and differential adsorption energies (based on the most stable configuration at lower coverage) of various NO* configurations at 7/9 – 1 ML NO*.

Calculations of saturated NO* + H* surfaces were also carried out at 0 – 1 ML NO* to determine enthalpies and free energies of replacing an NO* with H* on the catalyst surface:

$$NO^* + \tfrac{1}{2}\,H_2\,(g) \rightarrow H^* + NO(g)$$

Replacing NO* with H* on the surface has a negative ΔΔG at high NO* coverages (≥ 5/9 ML NO*) and positive ΔΔG values at lower NO* coverages. It is exothermic at high NO* coverages (≥ 7/9 ML NO*) but becomes endothermic at lower NO* coverages. The ΔΔG from measured β values is 14 kJ mol^{-1}, similar to the value calculated at 4/9 ML NO* (16 kJ mol^{-1}), but the ΔΔH from the temperature-dependence of β is 21 kJ mol^{-1}, closest to the DFT-predicted value at 5/9 ML NO* (36 kJ mol^{-1}), but. Changes in entropy (ΔΔS) were ≥ 72 J mol^{-1} K^{-1}, significantly higher than that derived from the temperature-dependence of β (18 J mol^{-1} K^{-1}).

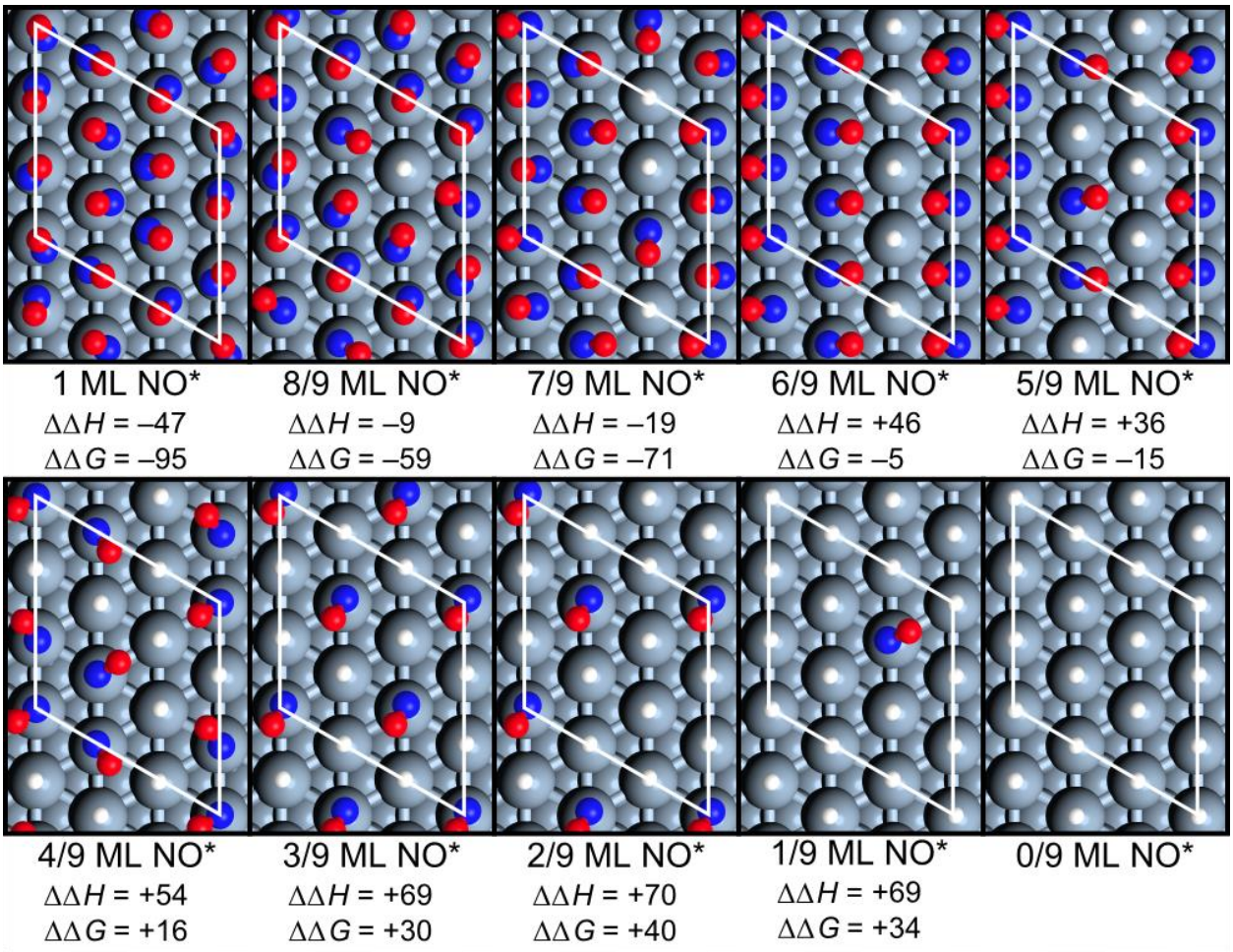

Figure S14. DFT-calculated structures and differences in adsorption energies of saturated NO* and H* surfaces at 0 – 1 ML NO*.

S5. Structural Images and Details of Density Functional Theory Calculations

I) **$2\ NO^* \rightarrow N_2O + O^* + *$**

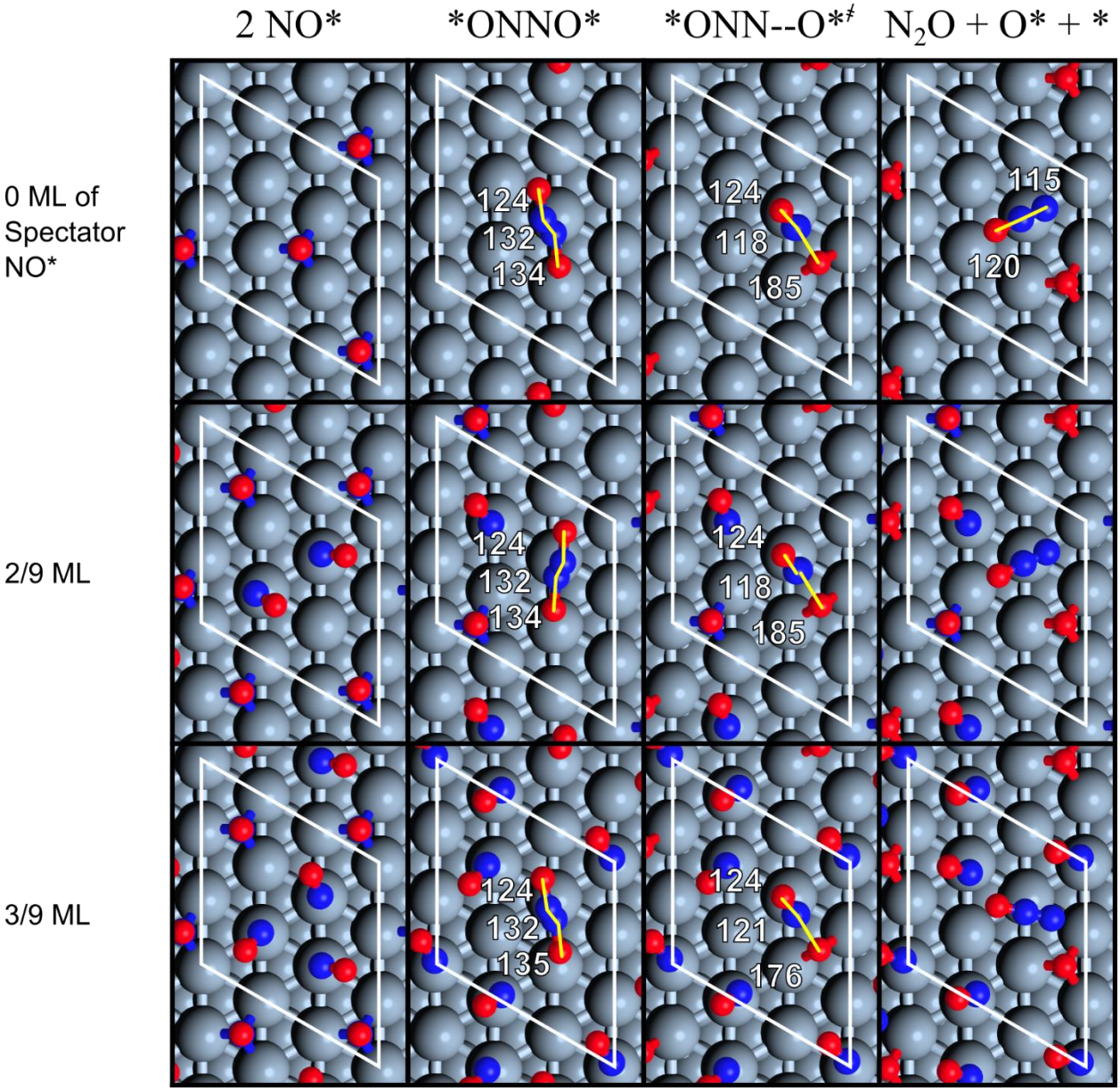

Figure S15. DFT-calculated reactant, product, and transition state structures for NO*-assisted NO* dissociation to form N_2O and O* at 0 – 3/9 coverage of spectator NO*. O-N, N-N, and N-O bond lengths are shown in pm for *ONNO* and transition states. N_2O product geometry is shown at 0 ML of spectator NO* coverage and does not vary.

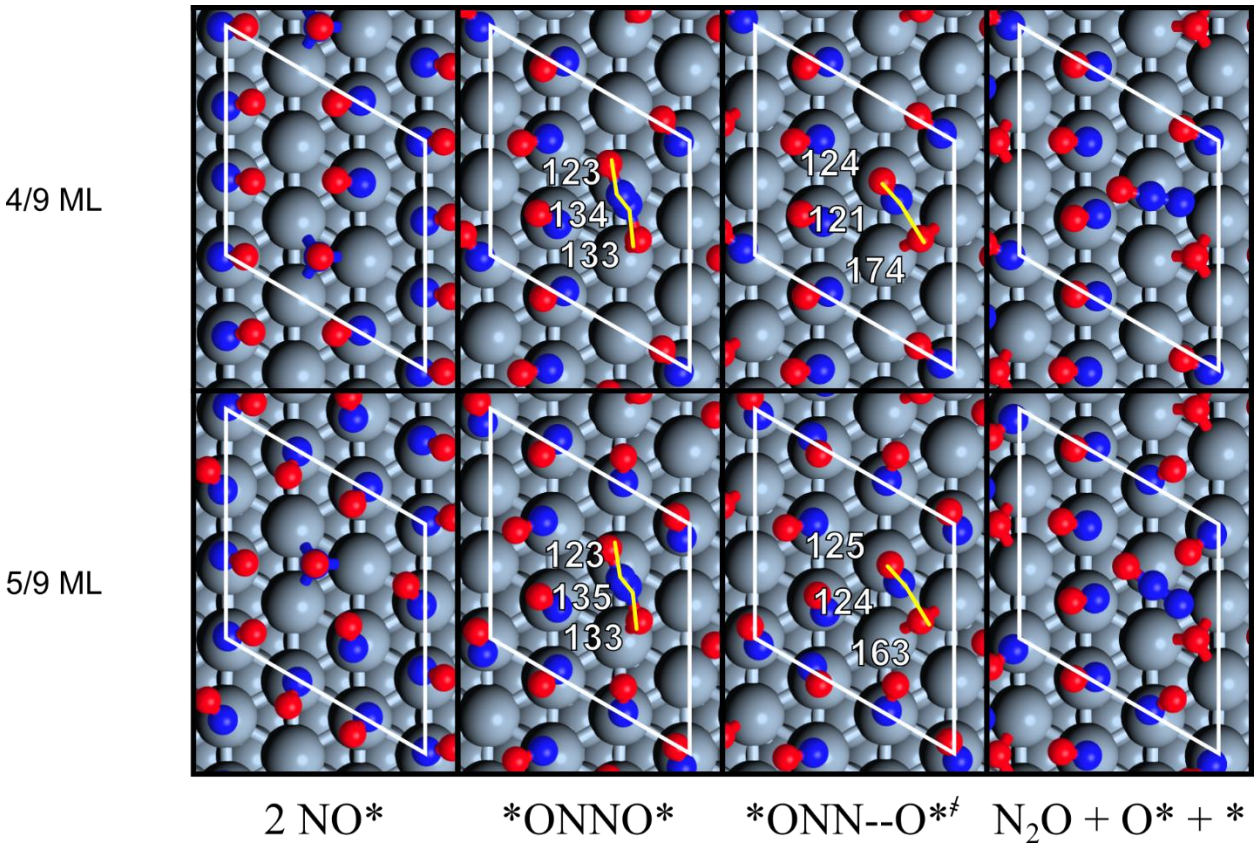

Figure S16. DFT-calculated reactant, product, and transition state structures for NO*-assisted NO* dissociation to form N_2O and O* at 4/9 – 5/9 coverage of spectator NO*. O-N, N-N, and N-O bond lengths are shown in pm for *ONNO* and transition states. N_2O product geometry is shown at 0 ML of spectator NO* coverage and does not vary.

NO*-assisted NO* dissociation was modeled at 0 – 5/9 ML of spectator NO* coverage (2/9 – 7/9 ML of total NO*) (Figs. S15-S16). Calculations without spectator NO* indicated that during this reaction, an *ONNO* intermediate is formed and that activating the N-O bond of this species is the relevant transition state for the overall reaction. Calculations at higher coverages were then modeled simply as:

$$*ONNO* \rightarrow N_2O + O* + *$$

Thus, the 2 NO* state was not explicitly modeled during this calculation, as that state had been previously modeled during examination of NO* coverage effects, shown above, and the 2NO* state for high coverages are based on the calculations presented in Figs. S7-S9, shown here for convenience.

The N-O bond activation transition state shows an elongated N-O bond, which decreases in length as the coverage increases (185 pm at 0/9 ML to 163 pm at 5/9 ML), likely due to repulsions from spectator NO* which favor a smaller transition state. The N-N bond is also significantly shorter in the transition state (avg. of 121 pm) than in the *ONNO* state (avg. of 133 pm), indicating that the rehybridization of the N-atoms occurs at the same time as N-O activation. The N_2O product desorbs immediately because none of its atoms are interacting with the metal in the transition state and its geometry (shown in Fig. S15) is thus independent of coverage.

II) **NO* + * → N* + O***

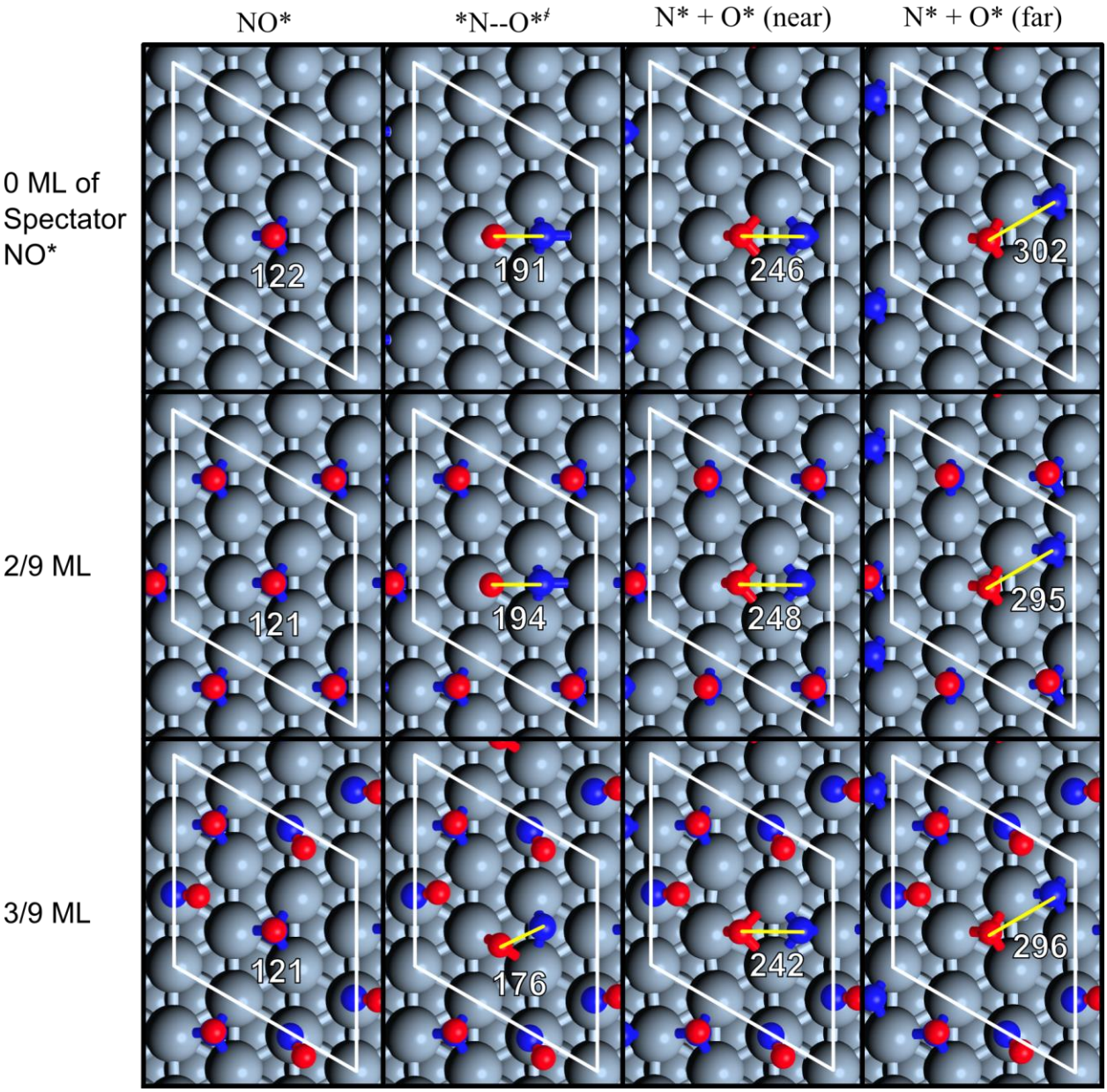

Figure S17. DFT-calculated reactant, product, and transition state structures for direct NO* dissociation to form N* and O* (prior to and following N* diffusion) at 0 – 3/9 coverage of spectator NO*. N-O bond lengths are shown in pm.

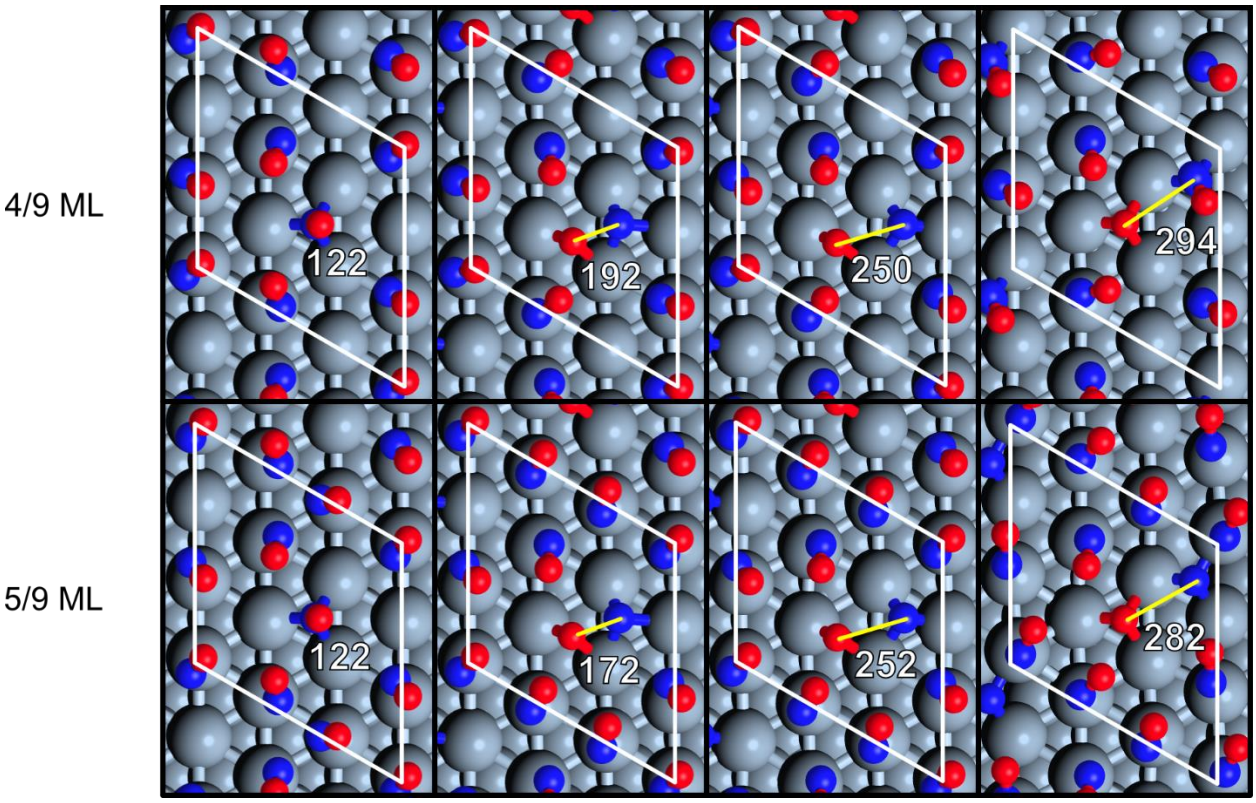

Figure S18. DFT-calculated reactant, product, and transition state structures for direct NO* dissociation to form N* and O* (prior to and following N* diffusion) at 4/9 – 5/9 coverage of spectator NO*. N-O bond lengths are shown in pm.

Direct NO* dissociation was modeled at 0 – 5/9 coverage of spectator NO* (Fig. S17-S18). At each NO* coverage, the most stable orientation of NO* was used as the reactant state (see above for examinations of various NO*-configurations at NO* coverages of 1/9 – 1 ML). The transition state geometry at low coverage (0 – 2/9 ML) has an elongated N-O bond (average of 193 pm) compared to the N-O bond in the reactant state (122 pm) and the O-atom of NO* is bound to one metal atom (192 pm) and the N-atom is bound strongly to two metal atoms (197 pm) and weakly to a third (244 pm). The transition state geometry changes at higher coverages (3/9 – 5/9 ML) due to repulsive interactions with spectator NO* species; the N-O bond is still elongated, but less dramatically (176, 192, and 172 pm for 3/9, 4/9 and 5/9 ML, respectively) and the O-atom has moved from a near-atop position at low coverage to an asymmetric bridging position (220 and 202 pm). The N* + O* (near) state shown is very unstable due to large repulsive interactions between N* and O*. From this state, the N* irreversibly diffuses away from the O* and rapidly undergoes secondary reactions. During optimization of the N* + O* (far) state for a coverage of 4/9 ML, N* reacted with a nearby NO* to form N_2O*, indicating the ease of N_2O* formation but an otherwise irrelevant outcome of the calculation as it has no bearing on the transition state.

III) NO* + H* → NOH* + * → N* + OH*

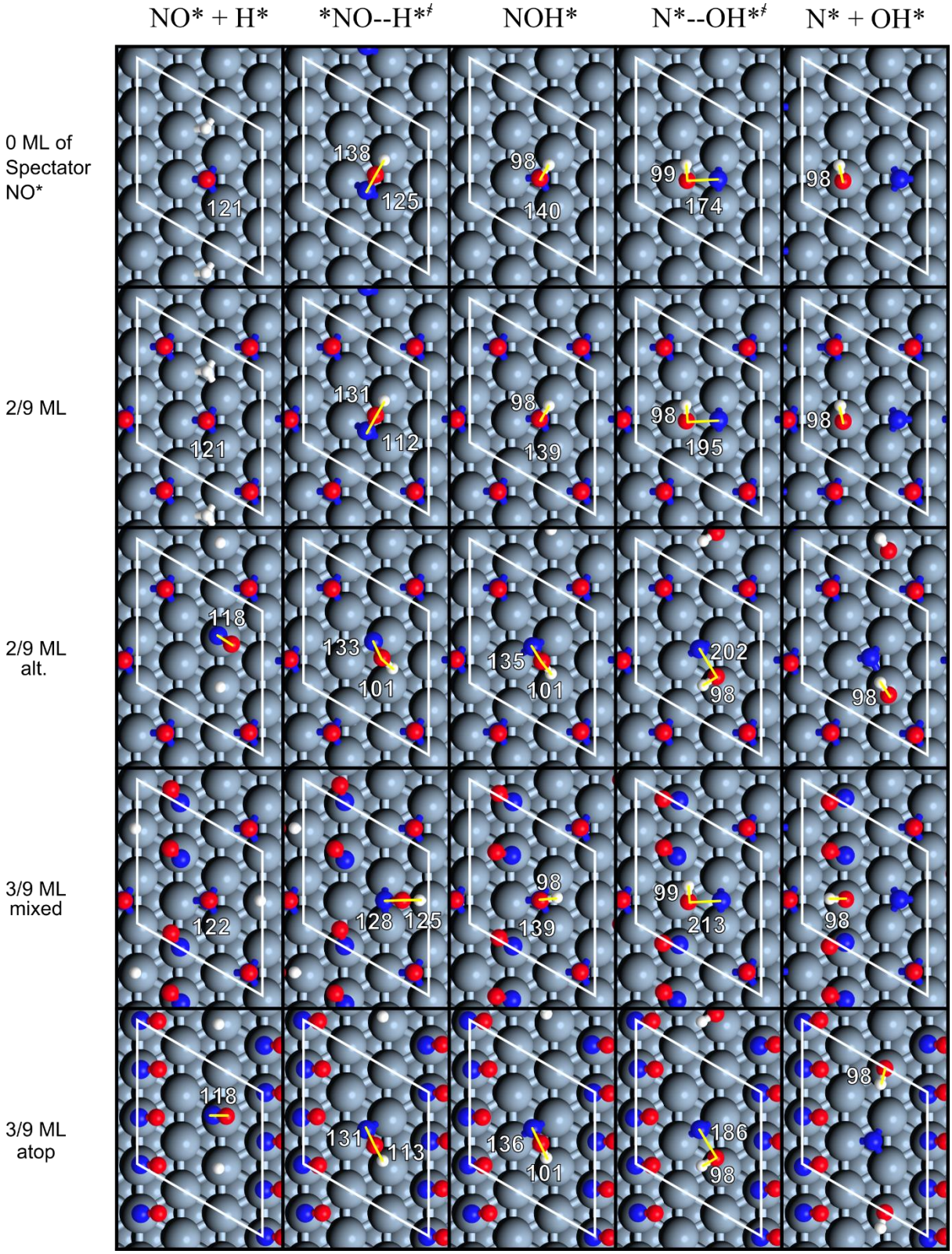

Figure S19. DFT-calculated reactant, product, and transition state structures for NOH* formation from H* and NO* and subsequent dissociation at 0 – 3/9 coverage of spectator NO*. O-H and N-O bond lengths are shown in pm.

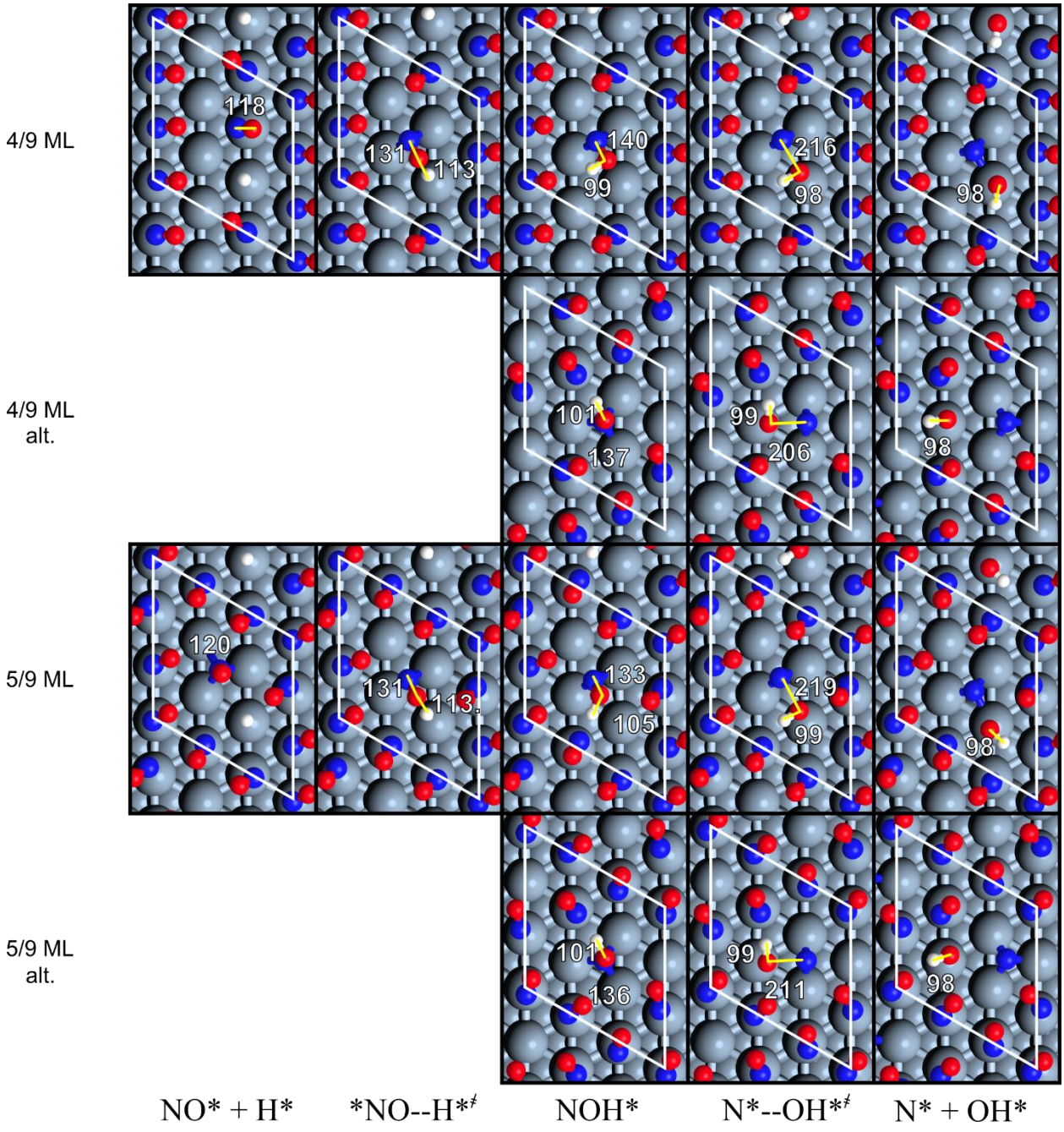

Figure S20. DFT-calculated reactant, product, and transition state structures for NOH* formation from H* and NO* and subsequent dissociation at 4/9 – 5/9 coverage of spectator NO*. O-H and N-O bond lengths are shown in pm.

The energetics of NOH* formation and dissociation were calculated at 0 – 5/9 coverage of spectator NO* (Figs. S19-S20). At 0 ML of spectator NO*, the NOH* formation transition state consists of a bridge bound NO* leaning towards the surface, forming a bond with an atop-bound H* (the O-H* bond is 125 pm in the transition state). NOH* then adsorbs in a three-fold fcc site, very similar to the NO* reactant, but the N-O bond has significantly lengthened (121 to 140 pm).

NOH* then dissociates via a transition state in which the N-atom is in a bridging position and OH* is in an atop position, the N-O bond is 174 pm in the transition state. The N* and OH* products adsorb in three-fold fcc and atop sties, respectively, with OH* having a bond length of 98 pm at all coverages. At 2/9 ML, two configurations of reactants were considered, one in which the NO* and H* were initially bound in three-fold sites and one where they are bound to atop sites. The three-fold state includes metal-atom-sharing between NO* and H*, and as previously discussed in Section SXX, metal-atom sharing significantly destabilizes the intermediates. Thus, the three-fold state has a higher free energy than the atop state (by 8 kJ mol^{-1}). The transition state for NOH* formation, however, prefers to bind with the NO* fragment bound in a bridge site, as was the case at 0/9 ML, and a transition state with this geometry was found starting from the three-fold state of the reactants. As discussed in the manuscript, NOH* formation is quasi-equilibrated during this reaction, thus the transition state for NOH* dissociation is kinetically relevant for this pathway. This transition state structures for NOH* dissociation had free energies within 1 kJ mol^{-1} of one another, despite slightly different geometries (Fig. S19). Two configurations were considered at 3/9 ML, one in which the reacting NO* and one spectator NO* were bound three-fold ("mixed") and one in which all NO* were bound atop (Fig. S19). The NOH* formation and dissociation transition states had lower free energies in the "mixed" configuration (by 60 and 27 kJ mol^{-1}) because of the preference of 4/9 coverage of NO* to bind in a mixed configuration on Pt (as discussed in Section S4). Two configurations were considered at 4/9 and 5/9 ML coverage as well, in each case, the more stable NOH* dissociation transition states are shown in Fig. S20, with the less-stable ones shown as "alt". All spectator NO* are bound atop at these two coverages, so differences in transition state stabilities reflect changes in energy upon NO* rotation to minimize repulsions, as shown at high coverages in Section S4.

IV) NO* + H* → HNO* + *

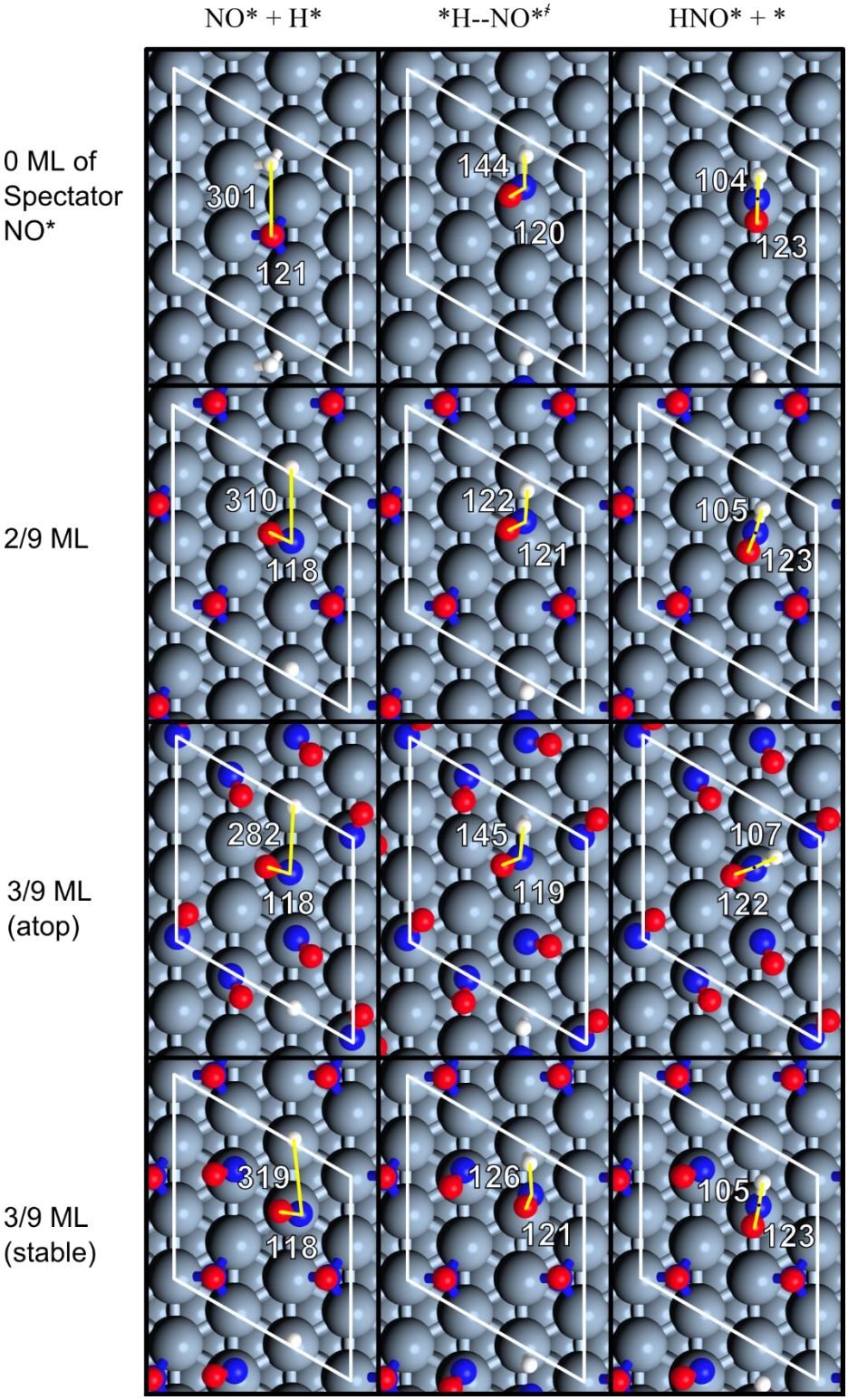

Figure S21. DFT-calculated reactant, product, and transition state structures for HNO* formation from H* and NO* at 0 – 3/9 coverage of spectator NO*. H-N and N-O bond lengths are shown in pm.

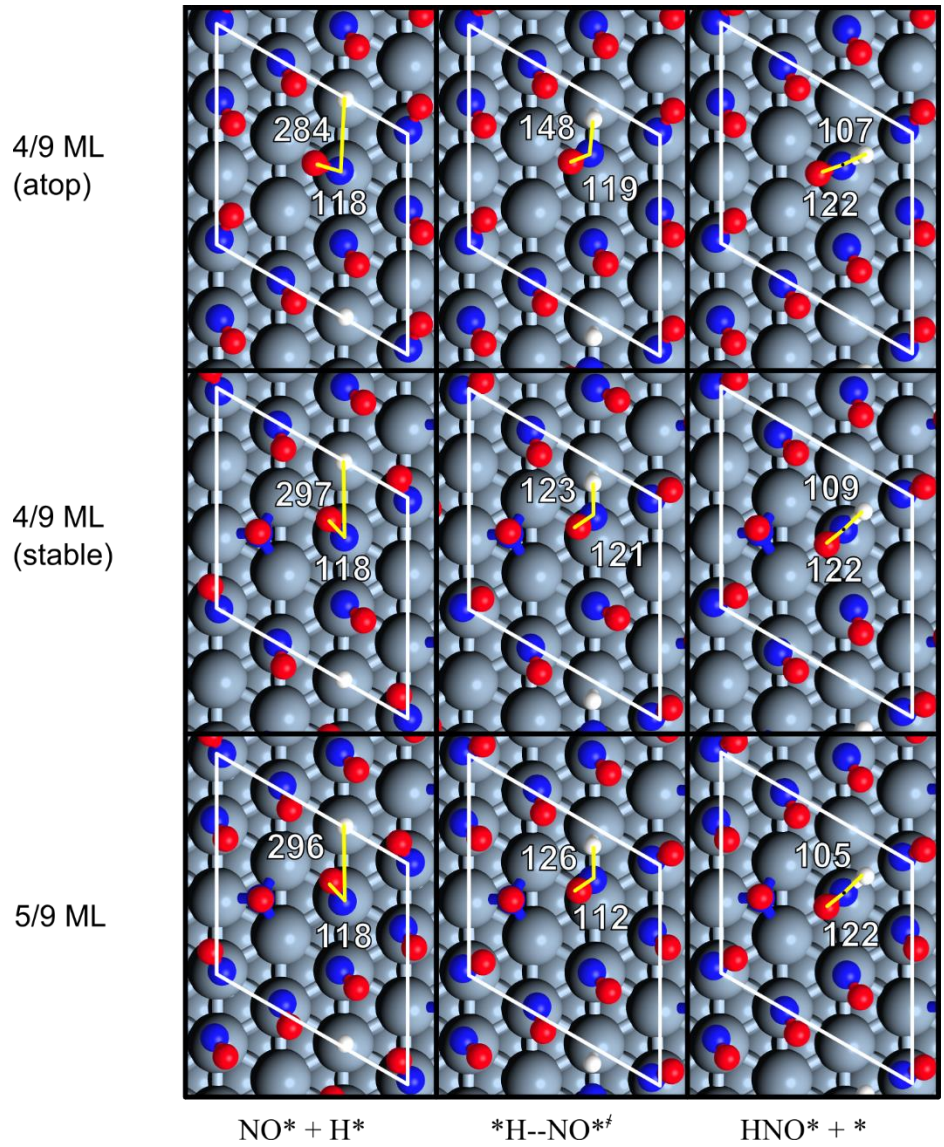

Figure S22. DFT-calculated reactant, product, and transition state structures for HNO* formation from H* and NO* at 4/9 – 5/9 coverage of spectator NO*. H-N and N-O bond lengths are shown in pm.

The energetics for HNO* formation were calculated at 0 – 5/9 coverage of spectator NO* (Fig. S22-23). At each NO* coverage, the most stable orientation of NO* with a vacant atop site (for H* adsorption) was modeled as the reactant state. For 3/9 and 4/9 ML of spectator NO*, additional configurations of NO* were examined which consisted entirely of atop-bound NO* species. The transition states at these additional configurations (shown in Fig. S21-22 denoted "atop") had free energies 15 and 30 kJ mol^{-1} higher (less stable), respectively, than those containing more stable NO* configurations in which some NO* are bound to 3-fold sites and some to atop sites. Among these configurations, transition state geometries are essentially unaffected by spectator NO* coverage, with N-H bond lengths near 125 pm, however, the atop configurations (modeled for 3/9 and 4/9 ML only) had N-H bond lengths in the transition state near 147 pm, significantly longer.

V) HNO* + H* → *HNOH* → NH* + OH*

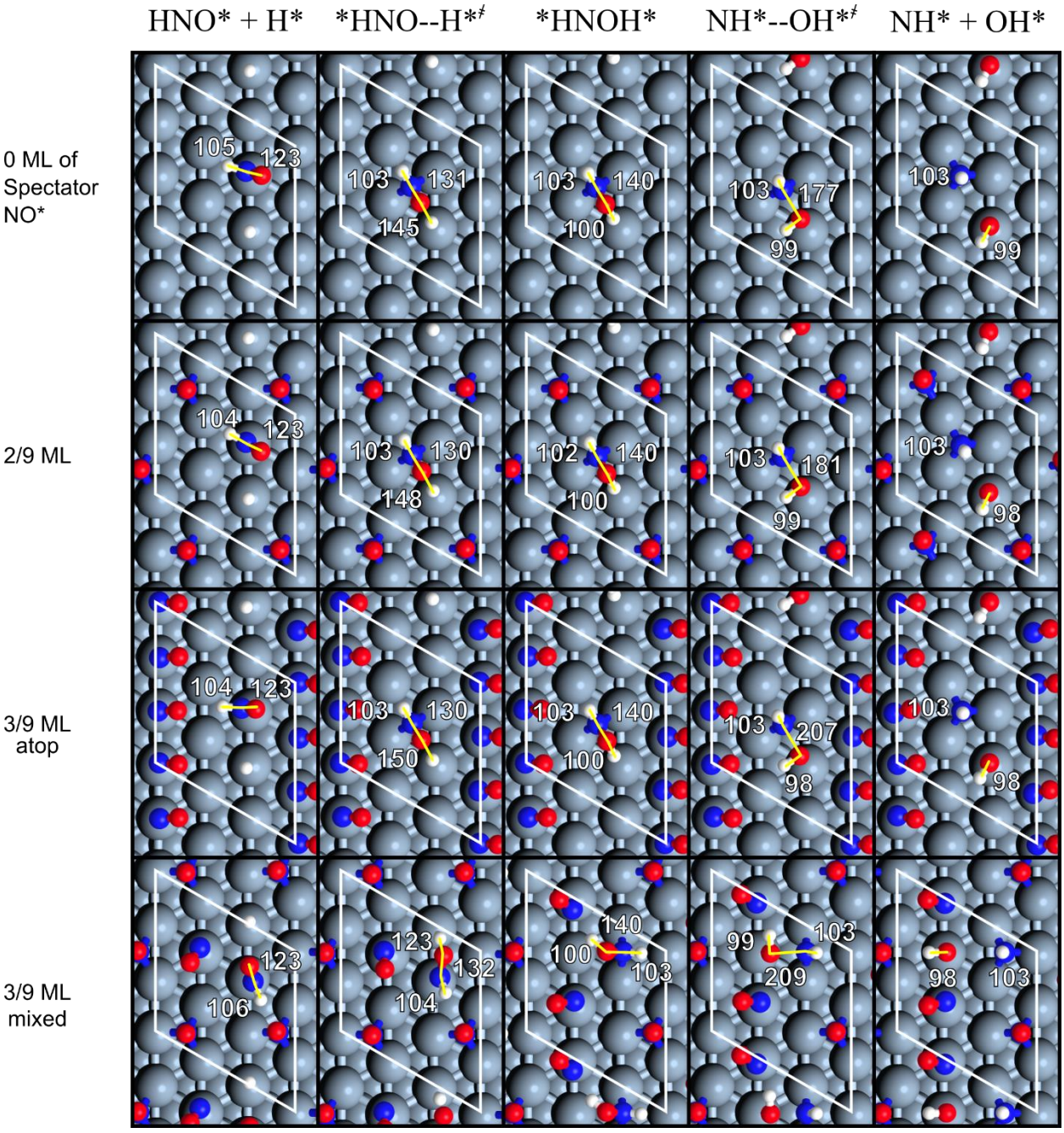

Figure S23. DFT-calculated reactant, product, and transition state structures for *HNOH* formation and dissociation at 0 – 3/9 coverage of spectator NO*. N-H, O-H and N-O bond lengths are shown in pm.

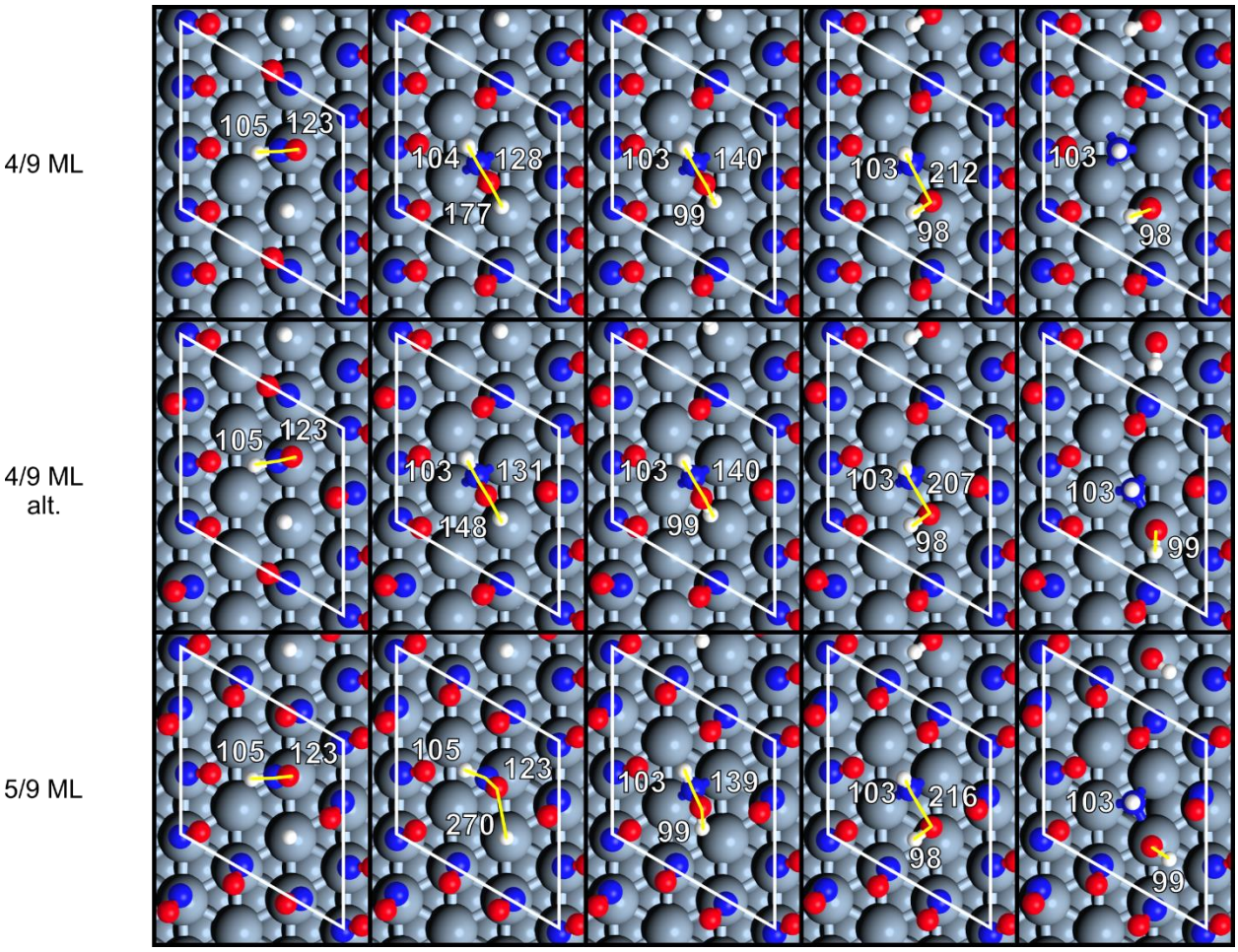

Figure S24. DFT-calculated reactant, product, and transition state structures for *HNOH* formation and dissociation at 4/9 – 5/9 coverage of spectator NO*. N-H, O-H and N-O bond lengths are shown in pm.

The energetics of *HNOH* formation (from HNO* and H*) and dissociation (into NH* and OH*) were calculated at 0 – 5/9 ML of spectator NO* (Figs. S23-S24). Transition states for *HNOH* formation and dissociation are structurally similar to those observed for NOH* formation and dissociation (Figs. S19-S20) in which the HNO* species is bound to a bridge site, interacting with an atop H* during *HNOH* formation and the NH* species is bound to a bridge site with OH* in an atop site during *HNOH* dissociation. Multiple configurations of spectator NO* were considered at 3/9 – 4/9 ML. At 3/9 ML, the configuration that consisted of spectator NO* in atop positions was less stable (by free energies of 35 and 18 kJ mol^{-1} for the formation and dissociation transition states) than one in which spectator NO* occupied atop and three-fold positions. Changes in NO* configuration at 4/9 ML had little impact on free energies of transition states, with the *HNOH* formation transition state being within 1 kJ mol^{-1} at each configuration and the *HNOH* dissociation transition state being 5 kJ mol^{-1} less stable with spectator NO* in the "alt" position (Fig. S24). At 5/9 ML of NO* coverage, the transition state for *HNOH* formation is associated

with HNO* diffusion into the bridging site (hence the different geometry shown in Fig. S24), which has a slightly higher barrier than HNOH* dissociation (Fig. 16).

S6. Regressions for NO-H_2 and NO-D_2 Kinetic Isotope Effect Studies

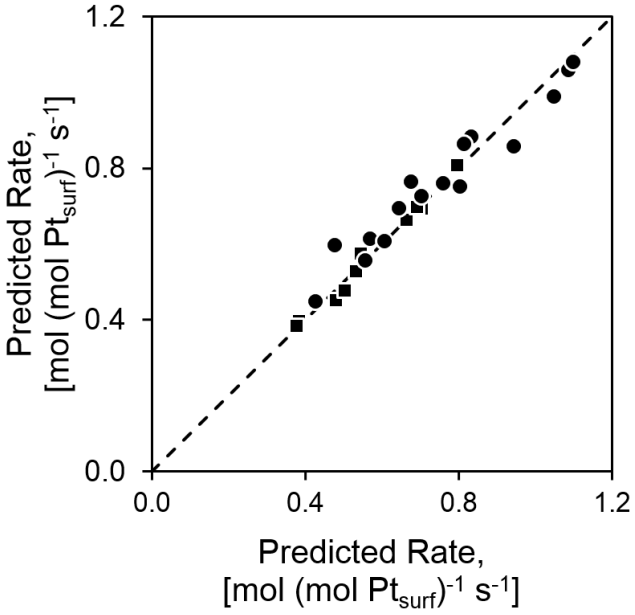

Figure S25. Measured and predicted NO activation turnover rates (Eq. 23) with kinetic parameters shown in Table S2 for NO-H_2 (●) and NO-D_2 (■) reactions at 423 K on 0.6% Pt/Al_2O_3 (4.4 nm average particle diameter), 1–3 kPa H_2, 3–12 kPa D_2, 0.1–0.5 kPa NO, 5-25 $cm^3s^{-1}g^{-1}$.

Table S2. Regressed kinetic parameters for Equation 23.

	α s^{-1}	β $kPa^{-0.5}$
H_2	0.419 ± 0.05	0.206 ± 0.027
D_2	0.303 ± 0.04	0.324 ± 0.029